Journal of Materials Chemistry A

RSC Publishing

PAPER

View Article Online
View Journal | View Issue

Cite this: *J. Mater. Chem. A*, 2013, **1**, 7091

Introducing nanocrystalline CeO_2 as heterogeneous environmental friendly catalyst for the aerobic oxidation of *para*-xylene to terephthalic acid in water†

Kalyanjyoti Deori, Dinesh Gupta, Basudeb Saha,* Satish K. Awasthi and Sasanka Deka*

Received 20th December 2012
Accepted 28th March 2013

DOI: 10.1039/c3ta01590d

www.rsc.org/MaterialsA

CeO_2 nanoparticles exposed in (100) and (111) surfaces have been synthesized and explored as a heterogeneous catalyst for the first time in the oxidation of *para*-xylene to terephthalic acid. The synthesis and catalysis reaction was environmental friendly, where water was used as the solvent. Ceria nanoparticles were synthesized with controlled size of 15 nm and high surface area of 268 $m^2\ g^{-1}$ magnitude. These particles were exploited as a novel heterogeneous catalyst for aqueous phase oxidation of *para*-xylene to bypass all the hazardous steps involve in the manufacture of industrially important terephthalic acid. The result shows the formation of 30–40% terephthalic acid under mild reaction condition, *i.e.* at 70 °C in water, by avoiding the corrosive bromide promoter and acetic acid solvent. The recyclability studies reveal that the recovered ceria catalyst retained its activity in *para*-xylene conversion without the change in the fluorite crystal structure, crystallite size and morphology of CeO_2. At last, a radical mechanism for this particular catalytic activity of the catalysis reaction has been proposed based on the high surface area and the corresponding available exposed active (100) and (111) surfaces.

Introduction

The development of an environmentally friendly, low cost and still highly efficient heterogeneous catalyst for the production of commodity chemical terephthalic acid (benzene-1,4-dicarboxylic acid) from the aerobic oxidation of *para*-xylene is an important area of industrial research. Terephthalic acid is widely used in the manufacture of polyesters, commonly by the reaction with ethylene glycol to produce polyethylene terephthalate (PET) which is then converted to fiber, film, containers, packaging materials, molded articles and household consumable goods.[1] In commercial practice, terephthalic acid is commonly made by liquid phase oxidation of *para*-xylene in acetic acid solvent with air or other source of oxygen in the presence of a bromide-promoted homogeneous catalyst comprising cobalt(II) acetate, manganese(II) acetate and hydrobromic acid under typical reaction conditions of 150–220 °C and 20–25 bar.[2–6] Major drawbacks in the synthesis of terephthalic acid by such process arise from the use of hydrobromic acid as a promoter.[4,5] Few recent reports[7] describe that the bromide promoter used with the catalyst corrodes the expensive titanium reactor and formed environmentally hazardous methyl bromide as a by-product.

However, in the absence of hydrobromic acid promoter in a conventional cobalt–manganese catalyst, *para*-xylene oxidation is very slow and the oxidation of acetic acid solvent to carbon dioxide and carbon monoxide tends to increase in the absence of bromide promoter.[7] Although several alternate promoters have been reported as potential replacement for hydrobromic acid in the conventional cobalt–manganese homogeneous catalytic system, including *N*-hydroxyphthalimide[8] and bromoanthracenes,[9] these alternatives are not practical either because of their consumption or decomposition.

Liquid phase selective oxidation of *para*-xylene to terephthalic acid by oxo-bridged cobalt–manganese complexes encapsulated in zeolite-Y has been tested in acetic acid solvent by Ratnasamy *et al.*[10] However, oxidation of acetic acid to unwanted green house gases remains an issue in their process. The use of heterogeneous catalysts consisting of palladium, antimony and molybdenum loaded on a titania support in combination with several other metal acetates have been reported in an international patent.[11] Although the patent claimed relatively high conversion of *para*-xylene and high selectivity in terephthalic acid product, the recyclability of the catalyst remains a concern in the patent. Utilization of supercritical water for effective oxidation of *para*-xylene to

Department of Chemistry, University of Delhi, Delhi-110007, India. E-mail: bsaha@chemistry.du.ac.in; sdeka@chemistry.du.ac.in; Tel: +91-11-27666646

† Electronic supplementary information (ESI) available: Few additional TEM/HRTEM images, O_2 consumption curve as a function of time for the oxidation of *para*-xylene, HPLC chromatogram of the product solution, powder XRD pattern and TEM images of the recovered ceria, initial rates for aerobic oxidation, FT-IR spectra of as-synthesized fresh catalyst and recovered catalyst. See DOI: 10.1039/c3ta01590d

terephthalic acid using O_2 as oxidant has also been reported, but this process at high temperature (300–400 °C) could be energy intensive for large scale production.[12] Therefore, the development of an environmentally friendly, low cost, recyclable and still highly efficient heterogeneous catalyst for the aerobic oxidation of *para*-xylene to terephthalic acid is essential from both economic and environmental point of view.

CeO_2 is one of the mostly studied and widely applied oxide material in both bulk and nanoparticle form. The synthesis and applications of this rare earth oxide have been already discussed in various recent review articles.[13–15] CeO_2 particles of either isotropic or anisotropic shape (with or without metal nanoparticles support) are coveted in a variety of applications, *e.g.* ceramic ingredient,[16] oxygen gas sensors,[17] methanol oxidation,[18,19] chemical–mechanical polishing agent,[20] toluene oxidation,[21] catalyst for the exhaust gas treatment from automobiles,[22] in solid oxide fuel cells,[23] CO oxidation,[24,25] production of H_2,[26] and many more. However, to the best of our knowledge the catalytic application of single CeO_2 particle (either in bulk or nano or doped) in the oxidation of *para*-xylene to terephthalic acid is not known. Cerium(IV) oxide crystallizes in most stable fluorite phase with a face centered cubic lattice. In most of the catalytic applications of CeO_2 for other type of reactions, it has been noticed that an increased catalytic activity comes from several defects which depend on partial pressure of oxygen.[11–14] The principal defects of interest are oxygen vacancies and small polarons (electrons localized on cerium cations) because these two are located in the "useful" range of ceria. In the case of oxygen defects, the increased diffusion rate of oxygen in the lattice causes increased catalytic activity as well as an increase in ionic conductivity, making ceria an interesting candidate as catalyst in various important reactions. Moreover, most of the reports on the catalytic activity of CeO_2 reported preferential activity of exposed (100), (110) and (111) surfaces.[27] Either these surfaces have high preference towards the reactants or have high physisorption and chemisorption rate or act as stable support for other material.

The present paper demonstrates the synthesis of (100) and (111) surface exposed size controlled CeO_2 nanocrystals (NCs) and their catalytic application in the aerobic oxidation of *para*-xylene to terephthalic acid in environment friendly conditions. Monodispersed CeO_2 nanocrystals of 15 nm have been synthesized using a novel solvothermal technique. HRTEM analysis revealed that these single crystalline particles are exposed with (111) and (100) surfaces. The liquid phase aerobic oxidation of *para*-xylene with molecular oxygen was carried out in water as a solvent under mild reaction condition at a temperature in the range from 40 °C to 95 °C and one bar oxygen pressure. Bromide ion promoter was not used in the present oxidation process, unlike conventional commercial catalysts and process for making terephthalic acid in acetic acid solvent in which reactive bromide promoter is used. An optimized reaction condition was developed by performing the reactions at several reaction variables including catalyst dosages, reaction time and temperature, and by comparing the rate of oxygen consumption. Detailed product analysis of the reaction mixture was performed by HPLC method. The results revealed moderate to excellent *para*-xylene conversion and moderate selectivity in the desired product for the reactions carried out at 70 °C. Because of the heterogeneity of the catalyst, it was recovered from the liquid reaction mixture, washed, dried and reused without a significant loss in activity. Thus the main motivation of the present synthesis of CeO_2 nanocrystals with a controlled size and morphology is the possibility of developing catalytic materials having high surface area and well-defined exposed crystal planes that exhibit best catalytic activity.

Experimental details

Chemicals

Cerium(III) chloride heptahydrate ($CeCl_3 \cdot 7H_2O$, 99.9%) was purchased from Sigma-Aldrich, USA. Cetyl tri-methyl ammonium bromide (CTAB, 99%) and ethylene diamine (1,2-diaminoethane) (99%) were purchased from SRL-India. Absolute ethanol (C_2H_5OH) (99.9%) was purchased from Changshu Yangyuan chemical, China. Commercial CeO_2 of particle size <5 μm and 99.9% purity was obtained from Sigma-Aldrich, USA. Standard *para*-xylene, terephthalic acid, 4-carboxybenzaldehyde, *p*-toluic acid, terephthaldialdehyde samples were purchased from Sigma-Aldrich, USA. All chemicals were used as received without further purification. In a typical synthesis procedure, 1.5 mmol CTAB was dissolved in a mixture of polar solvents *i.e.* water and ethanol (15 mL each) and then 0.5 mmol of $CeCl_3 \cdot 7H_2O$ was added to this solution (CTAB to $CeCl_3 \cdot 7H_2O$ ratio was 3 : 1). The reaction mixture was continuously stirred for 1 hour by magnetic stirrer and then 15 mL of ethylenediammine (en) was added drop wise under vigorous stirring and kept stirring for another 1 hour till yellow color appeared. The yellow solution was then finally transferred into a Teflon-lined stainless steel autoclave and the sealed autoclave was heated at 160 °C for 36 hours in a PID controlled oven, and then cooled to room temperature in air naturally. The as-obtained white precipitate was centrifuged and washed with distilled water and absolute ethanol for two times repeatedly. The experimental yield of this synthesis reaction is 91% which is determined after annealing the sample at high temperature to remove the surfactant. A small part of as-synthesized product was dispersed in 2 mL of ethanol and the remaining part of the product was oven dried at 40 °C in air and stored for further characterization and analyses.

Characterization

Transmission Electron Microscopy (TEM). Samples for TEM were prepared by dropping dilute solutions of nanocrystals onto carbon coated copper grids and letting the solvent evaporate. Low resolution TEM images, selected area electron diffraction (SAED) and Phase-contrast high-resolution TEM (HRTEM) measurements were performed with a Philips Technai $G^2$30 transmission electron microscope operating at an accelerating voltage of 300 kV.

Powder X-ray Diffraction (XRD). XRD measurements were performed with a Bruker D8 Advance and a Rigaku miniflex-(II) X-ray diffractometer employing monochromatized Cu Kα

radiation ($\lambda = 1.54056$ Å) at 298 K. Dry powder was spread on top of a glass substrate and was then measured in reflection geometry.

Field emission scanning electron microscopy (FESEM). SEM measurements for morphological characterization of the as-synthesized particles were done on a FEI Quanta 200F equipped with Oxford-EDS system IE 250 X Max 80. Thick concentrated sample solution was first drop casted on an ultrasonically cleaned ITO substrate letting the solvent evaporate.

Surface area and pore size. Surface area of samples were determined by Brunauer–Emmett–Teller (BET) principle and the pore parameters of the samples were determined by Barrett–Joyner–Halenda (BJH) method using 20 points BET equation with the help of Quantachrome instruments (Model NOVA 2000e surface area and pore size analyzer) at 77 K.

Fourier transform infrared spectroscopy (FT-IR). The FTIR spectra (KBr disk, 4000–400 cm^{-1}) were recorded on a Perkin-Elmer FTIR 2000 spectrophotometer.

Catalytic reactor and reaction. The progression of the oxidation reactions was monitored by the oxygen uptake method using a manometric apparatus for optimization of the reaction conditions.[2–6] The reactor, which contains an impeller to maintain oxygen saturation of the solution, was thermostated at 70 °C by means of a circulating water bath. Oxygen consumption was measured by monitoring the decrease in volume, at a constant 1 atm pressure of pure oxygen, in the manometer connected to the reactor. The initial reaction rates were calculated from the slope of the linear plots of the volume of oxygen consumption against time. Once optimized reaction conditions were developed, detailed product analysis of the reaction mixture was performed using a HPLC chromatograph equipped with an UV detector. The oxidation products were identified by their retention times in comparison with authentic samples.

Product identification by HPLC. Oxidation products of the catalysis reactions were monitored by HPLC, having calibrated the method with known compounds, qualitatively and quantitatively. For HPLC analysis, a 20 μL aliquot was removed from the reactor at different times during the reaction and diluted to 1 mL with 1 : 4 DMSO/CH_3OH (v/v). The diluted solution was then run through the HPLC column. A Shimadzu HPLC model SCL-10A VP equipped with UV-Vis detector (254 nm) and a C_{18}-4.6 × 250 reverse phase column was used for this method. A binary solvent of 50% H_2O/0.5% CH_3OH and 50% CH_3CN at flow rate 0.77 mL min^{-1} was used to analyze the sample in the isocratic mode. The oxidation products were identified by their retention times in comparison with authentic samples. Each peak of the HPLC chromatogram was properly integrated and the actual concentration of each component was obtained from the pre-calibrated plot of peak area against concentration.

Results and discussion

Structural and morphology studies of CeO_2 nanoparticles

The phase purity of the product obtained under the experimental condition (as introduced in the experimental section), was examined by the X-ray diffraction (XRD) measurements.

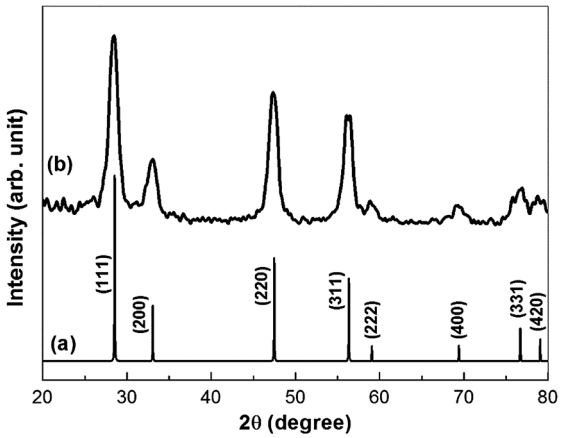

Fig. 1 (a) Bulk XRD pattern of cubic fluorite CeO_2 and (b) experimental XRD pattern of the as-synthesized nanoparticle sample.

Fig. 1 compares the XRD pattern of the as-synthesized sample to that of bulk CeO_2 (JCPDS card #34-0394). As shown in Fig. 1, the characteristic peaks located at $2\theta = 28.55$, 33.08, 47.49, 56.35, 59.09, 69.42, 76.71 and 79.08° are corresponding to (111), (200), (220), (311), (222), (400), (331) and (420) planes, respectively. All these peaks can be indexed to a face-centered cubic (fcc) pure phase of CeO_2 fluorite structure, which is purely matching with the bulk XRD pattern (Fig. 1a) and to the reported value (space group = *Fm*3*m*, space group no. = 225, $a = 5.411$ Å). The interesting information obtained in the XRD pattern of the as-synthesized CeO_2 is that the peak intensity ratios of (200)/(111) and (220)/(111) planes were higher than the bulk ceria. The peak intensity ratio of (200)/(111) in bulk CeO_2 is 0.26, where as the observed ratio for our CeO_2 NCs is 0.42. A similar trend is seen for the peak intensity ratio of (220)/(111) planes. The bulk intensity ratio is 0.55, whereas the observed ratio is 0.82 in the present study. These preliminary results suggests a better exposure of the active (100) and (110) surfaces relative to (111) surface in the present CeO_2 nanocrystals as compared to the bulk CeO_2 particles.

The calculated lattice parameter of the as-synthesized sample is found to be 5.410 Å, which is in good agreement with the JCPDS card values. No peaks of any other phases or any other impurities are detected, indicating the high purity of the CeO_2 cubic phase. The broad and sharp reflections in the XRD patterns suggest that the as-prepared CeO_2 nanoparticles are nanocrystalline in nature. The average crystallite size was calculated using the Scherrer formula, and found to be 13 nm.

The morphology of the as-prepared CeO_2 nanocrystals was first analyzed by TEM, and the results are shown in Fig. 2. It can be seen that the shape of all CeO_2 nanoparticles is close to hexagonal/spherical morphology with nearly monodispersed particles with some agglomeration due to the synthesis condition in aqueous media. The average particle size was measured around 15 nm which is consistent with the average size obtained from XRD measurements. The hexagonal morphology of the as-synthesized samples becomes more prominent in the upper inset (Fig. 2b), which shows few of the hexagonal images obtained under higher magnification. Spotty SAED pattern of

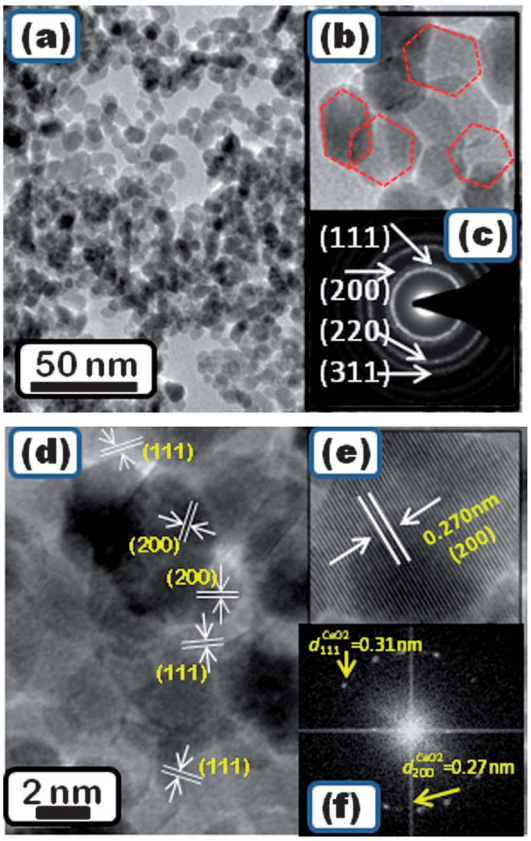

Fig. 2 (a) Low magnification TEM image, (b) high magnification images of few hexagonal morphologies, (c) SAED pattern, (d) HRTEM image of as-synthesized CeO_2 nanoparticles with 15 nm size, (e) lattice fringes of a single CeO_2 nanocrystal and (f) 2-D Fast Fourier Transform (FFT) image of selected area from panel (d).

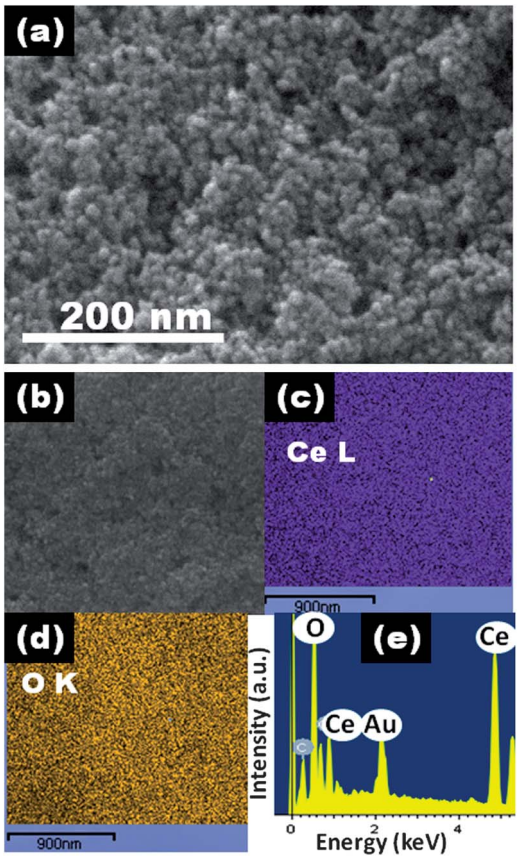

Fig. 3 (a) FESEM image of CeO_2 NCs sample. Stoichiometric characterization by SEM elemental mapping (b) CeO_2 particles, (c) Ce and (d) O (elemental mapping of Au, appeared due to gold coating of the sample during sample preparation is not shown) distribution in the sample. (e) Representative SEM-EDS spectrum of the as-synthesized CeO_2 particles selected randomly from different areas.

CeO_2 nanoparticles is shown as lower inset (Fig. 2c), revealing the pure crystalline nature of as-synthesized particles with cubic fluorite structure, where (111), (200), (220), and (311) lattice planes were clearly indexed. However, spotty rings were observed due to random orientations of single crystalline CeO_2 in the TEM grid in different directions. The structure of CeO_2 nanoparticles was further investigated by phase contrast HRTEM. The lattice and high crystallinity of CeO_2 nanocrystals are shown in Fig. 2d from few single nanocrystals. Distinctive set of fringes can be unambiguously identified, such as those corresponding to (111) planes of bulk fcc-CeO_2 (d_{111}^{CeO2} = 0.31 nm) and (200) planes of CeO_2 (d_{200}^{CeO2} = 0.27 nm). The clear lattice fringes from the phase-contrast HRTEM image indicated that the as-prepared CeO_2 was nearly free from dislocations and stacking faults and it is single crystalline in nature. The two-Dimensional Fast-Fourier Transform (2D-FFT) pattern calculated from the CeO_2 section seen in panel 'd' is shown as Fig. 2f. This also confirmed the presence of high energy (200) planes or growth of CeO_2 NCs in both [111] and [100] directions.

High resolution field emission SEM (FESEM) measurements were carried out to examine the size, morphology and composition of the as-synthesized ceria nanoparticles. FESEM image of CeO_2 nanoparticles shows (see Fig. 3a) an unclear shape having average size of 15 nm, which is close to the average particle size calculated from the corresponding XRD pattern using the Scherrer formula and also confronted by HRTEM analysis. Elemental mapping *via* EDS technique in SEM confirmed that both Ce and O were uniformly distributed among the nanocrystals, which means that there was no appreciable compositional variation among them (Fig. 3c and d). The Energy Dispersive X-ray Spectroscopy (EDS) spectra taken from CeO_2 particles over a very large area (2 μm × 2 μm, Fig. 3e) revealed the particles to be of pure cerium oxide having only Ce and O. XRD and EDS analyses claimed the presence of only Ce and O elements in the as-synthesized sample, however because of the limitations of these techniques we cannot rule out the presence of anions (Cl^- and Br^-) which may be surface adsorbed. However, Wu *et al.* and Liu *et al.* reported independently that, the adsorption effect of these anions towards cerium oxide surface is very weak.[28] Therefore, based on the thorough washing, XRD and EDS analyses on different batches of CeO_2 NCs we could neglect the possibility of the presence of trace amount of anions in the final sample. Elemental analysis revealed an average O/Ce ratio over different regions of 2.0–2.5. The presence of excess oxygen cannot be ruled out due to oxygen containing surfactants as well as adsorbed oxygen molecules in pores.

Surface area and pore size/volume of CeO_2 nanoparticles

Since our aim of the present work was to establish the as-synthesized CeO_2 nanocrystals as a novel heterogeneous and environmental friendly catalyst for the aerobic oxidation of *para*-xylene to terephthalic acid in water, we have carried out a detailed N_2 adsorption–desorption study to find out available surface area for catalysis reaction as well as the pore size and pore volume. Fig. 4 shows the N_2 adsorption–desorption isotherms of the CeO_2 sample. The N_2 isotherm of the sample was of type IV and the hysteresis was a combination of type H2 and type H3, typical of a mesoporous sample.[29] Specific surface area was determined from the BET plot using the multipoint BET equation. A very high surface area of magnitude 268 $m^2\ g^{-1}$ was recorded for the as-synthesized CeO_2 NCs. An increase in surface area (268 $m^2\ g^{-1}$) is attributed to the reduction in particle size. Pore-size distribution curves calculated from the Barrett–Joyner–Halenda (BJH) method indicated the presence of mesoporosity, although they do not evidence the presence of regularly ordered pores (see inset in Fig. 4). A maximum pore distribution was observed at around 2–3 nm.

Catalytic study

The oxidation of *para*-xylene to terephthalic acid occurs through a complicated multi-step process. The stoichiometric equation is given below:

$$C_6H_4(CH_3)_2 + 3O_2 \rightarrow C_6H_4(COOH)_2 + 2H_2O \quad \text{(i)}$$

Several partially oxidized forms of *para*-xylene are produced during the course of free-radical chain reaction, namely *p*-tolualdehyde, *p*-toluic acid, terephthaldialdehyde (TPA) and 4-carboxybenzaldehyde (4-CBA).[1,4–6] Alcohol was not detected, presumably due to rapid oxidation of alcohols to aldehydes. The sequential oxidation process is shown below (Scheme 1).

Aerobic oxidation of *para*-xylene with molecular oxygen was carried out under mild reaction conditions using water as a solvent in the presence of CeO_2 NCs sample as catalysts. A preliminary reaction of *para*-xylene oxidation was carried out in a glass reactor using 6 mL water as a solvent under the condition of 100 mM *para*-xylene and 10 mg CeO_2 sample at 70 °C and 1 bar O_2 pressure. The progression of reaction for the preliminary experiments was monitored by the volume of O_2 consumption as a function of time for 8–10 h.[1,4,5] The initial change in the volume of O_2 against time was linear. The slope of the linear plot, when converted to concentration unit, gave the initial reaction rate as, $v_i = 31 \times 10^{-5}$ mol L^{-1} min^{-1}. The consumption of O_2 with times in the catalytic oxidation reaction is shown in Fig. S2 (ESI†). To confirm this catalytic effectiveness, a blank experiment was also performed for *para*-xylene oxidation without CeO_2 NCs sample, which showed no oxygen consumption in 10 h under identical reaction conditions. Thus, observed initial reaction rate in the presence of the CeO_2 material validated its catalytic effectiveness. To further test the effectiveness of the CeO_2 catalysts and optimize the reaction conditions, more experiments were designed at variable catalyst dosages and reaction temperatures. The results as summarized in Table 1, for the oxidation amounting to about 15–25% with respect to initial *para*-xylene concentration, showed an increase in v_i from 17×10^{-5} mol L^{-1} min^{-1} to 31×10^{-5} mol L^{-1} min^{-1} upon increasing the catalyst loading from 5 mg to 10 mg.

Further the batch oxidations of *para*-xylene with molecular oxygen were conducted in water using CeO_2 NCs sample. Two experiments were performed using a variable amount of catalyst and reaction time. The aliquot was collected after completion of reaction for the desired time and analyzed by HPLC chromatograph. Fig. 5 shows the results of the desired oxidation product along with partially oxidized intermediates. As seen in Fig. 5, *para*-xylene oxidation with 10 mg CeO_2 NCs sample under mild reaction condition produced 35% terephthalic acid in 25 h, along with partially oxidized intermediates, for example,

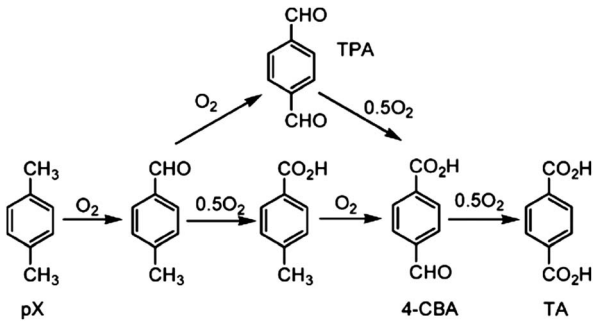

Scheme 1 Sequential oxidation process for *para*-xylene oxidation.

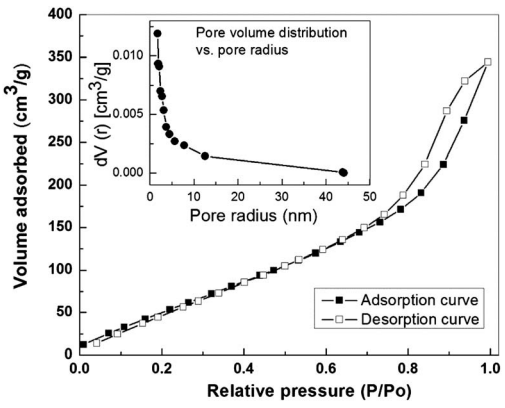

Fig. 4 N_2 adsorption–desorption isotherm of as-synthesized CeO_2 at 77 K. Inset: Pore volume distribution *vs.* pore radius of CeO_2 nanoparticles.

Table 1 Initial reaction rates for the CeO_2 catalyzed oxidation of *para*-xylene at variable temperatures and catalyst dosages

Entry no.	CeO_2 NCs (mg)	Temperature, °C	$v_i \times 10^{-5}$, mol L^{-1} min^{-1}
1	5	70	17
2	7.6	70	27
3	10	70	31
4	10	40	16
5	10	50	27
6	10	85	41

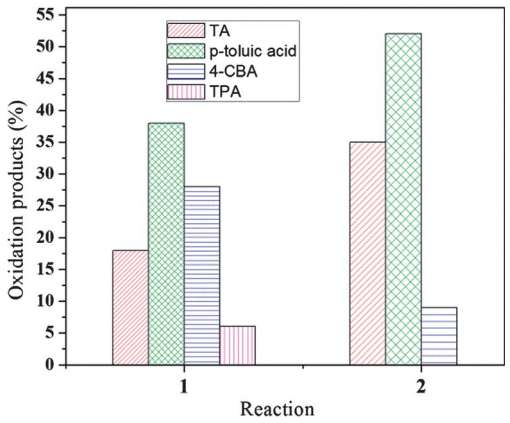

Fig. 5 Distribution of the reaction products for the oxidation of 100 mM *para*-xylene in water using 1 bar O_2 pressure under the conditions of (reaction 1) 10 mg CeO_2 NCs sample, $T = 85$ °C, time = 7 h and (reaction 2) 10 mg CeO_2 NCs sample, $T = 70$ °C, time = 25 h. (TA = terephthalic acid, 4-CBA = 4-carboxybenzaldehyde, TPA = terephthaldialdehyde).

52% *p*-toluic acid and 9% 4-carboxybenzaldehyde. Under similar reaction conditions, a control experiment using 10 mg commercially purchased CeO_2 (no preferred exposed surface) as a catalyst for 100 mM *para*-xylene oxidation at 85 °C for 8 h showed no evidence for terephthalic acid or other partially oxidized intermediates in the HPLC chromatogram (deposited in the ESI, Fig. S3†) of the product solution.

To further evaluate the effectiveness of the cerium oxide nanoparticulate catalyst at higher temperature, aerobic oxidation of 100 mM *para*-xylene with 10 mg CeO_2 NCs sample was carried out at higher temperature, *e.g.*, at 95 °C and 1 bar oxygen pressure using 6 mL water as a solvent. Fig. 6 shows the product distribution of the desired terephthalic acid along with other partially oxidized intermediates of *para*-xylene. Another reaction under similar conditions, but for a longer reaction time (24 h) produced more terephthalic acid (52%) along with 18% 4-CBA, 17% *p*-toluic acid and 7% TPA as partially oxidized intermediates. When the catalyst amount was tripled to 30 mg for 100 mM *para*-xylene oxidation at 95 °C for 12 h, the desired terephthalic acid yield improved to 61%. Other intermediate oxidation products were: 19% 4-CBA, 11% *p*-toluic acid and 6% TPA.

One important aspect of the present study is that the cerium oxide nanoparticulate catalyst can be recycled for the oxidation process. To examine the recyclability, the catalyst from a *para*-xylene oxidation reaction was recovered, washed, dried and reused for the next three cycles. The recycle experiment was performed under similar reaction conditions, as described in reaction 1 of Fig. 5, by adding fresh *para*-xylene substrate and water solvent. After 8 h reaction in each cycle, the aliquot was collected and analyzed by HPLC method. The results, as shown in Fig. 7, reveal that the catalyst retains its activity in the 4th cycle with only 2% loss in terephthalic acid yield in the 4th cycle. Additionally, the catalytic effectiveness of the recovered catalyst was further tested by measuring the ν_i values in each catalytic cycle. Fig. S4† shows that the ν_i values with the fresh catalyst and the re-used catalyst in the 4th cycle are 42×10^{-5} and 37×10^{-5} mol L^{-1} min^{-1}, respectively. To coincide with catalytic recyclability test, we performed further analyses to examine the phase and morphology of the recycled ceria nanoparticles. Detail powder-XRD and low-resolution-TEM images of the second (2nd) and fourth (4th) recycled CeO_2 nanoparticles are shown in ESI.† Fig. S5 and S6† show the retentivity of nanocrystalline nature of the recycled ceria (13–15 nm) with hexagonal morphology. There is no change in the fluorite crystal structure of the 2nd or 4th recycled samples.

Mechanism: the catalytic activity of CeO_2 nanocrystals

The catalyst used in the present study is an heterogeneous solid state catalyst in liquid environment. As established already, ceria in nanocrystalline form has more defects[30,31] as compared to the bulk form and as the crystallite size decreases, the number of oxygen vacancy increases. Thus, the increased diffusion rate of oxygen in the lattice causes an increased catalytic activity. In the present study the size of CeO_2 crystallite

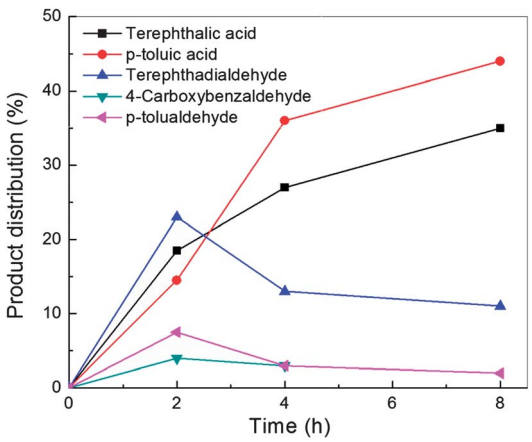

Fig. 6 Product distribution profile for aerobic oxidation of *para*-xylene with CeO_2 nanoparticles at 95 °C and 1 bar O_2 pressure.

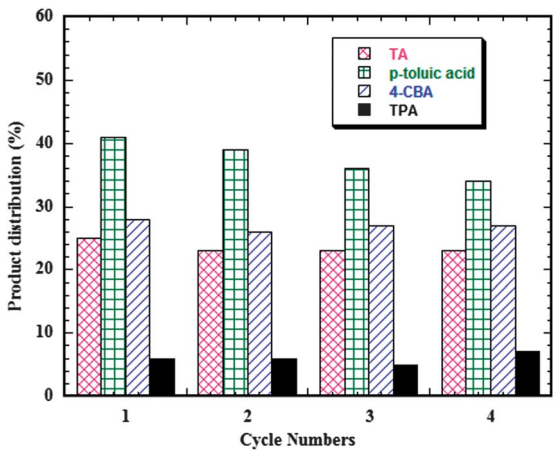

Fig. 7 Distribution of the reaction products for the oxidation of 100 mM *para*-xylene with the re-used catalyst in water. Other reaction conditions: 10 mg CeO_2 NCs recovered from the prior run, except the first cycle where fresh catalyst was used; $T = 85$ °C, time = 8 h.

is 15 nm, which have a very high BET surface area (as discussed in Fig. 4) and high number of pores in these smaller particles. Another reason for the higher catalytic activity of our ceria nanoparticles could be ascertain to the exposed (111) and (100) surface. Even though the (111) surface of CeO_2 is the most stable[27,32,33] and consequently the one which is predominantly exposed, at the same time it is comparatively less reactive with respect to (less stable) (110) and (100) surfaces. The energy required to create oxygen vacancies on the surface of CeO_2 (111), which is directly related to the Oxygen Storage Capacity (OSC) of the material, is greater as compared with that of CeO_2 (110) and (100). In the present study, from the HRTEM we found that the single crystalline CeO_2 particles are grown preponderantly in ⟨111⟩ and ⟨100⟩ direction. For the fcc cubic structure the energy of various low-indexed crystallographic planes are in order $\gamma_{\{111\}} < \gamma_{\{100\}} < \gamma_{\{110\}}$. The equilibrium shape of cubic lattice in the present case consists of (200) and (111) planes which occurred due to the growth in ⟨100⟩ and ⟨111⟩ directions, respectively, which is consistent with the crystallographic polyhedron shape observed by Dang *et al.*[34] In the present case also (200) face truncated octahedrons observed from the [100] direction are seen as polyhedron and are shown along with HRTEM images and 3D reconstructions in Fig. 8. However (100) surface is oxygen-terminated surface with half of the oxygen atoms moved from one surface to the other to fulfil the stoichiometric formula.[35] Thus, now we can explain the observation of less numbers of and/or truncated (200) planes and the observation of elongated hexagonal particles in both the samples (*e.g.* Fig. 2 and 8a and b). When we expect a growth along [100], we will see principally (111) planes at the top as shown in the 3-D reconstruction in Fig. 8. However, this growth along [100] could be ascertained by XRD analysis, as we obtained in the present case. Another major observation of this growth is the elongation of the particles or making elongated hexagonal particles (marked as 1–5 in Fig. 8a and b) along ⟨100⟩ direction. Thus observation of these elongated nanoparticles is the proof of presence of highly active (100) surfaces or {100} facets for high surface reactivity.

In water, the growth along [111] direction is energetically favored at low temperature, but at higher temperature, the growth along [100] direction is preferred as an increase in temperature is likely to promote the formation of {100} facets at the expense of {111} facets.[34,36,37] However, in the present study, the growth in [111] and [100] directions are favored due to the higher temperature as well as the presence of a surfactant (CTAB). We can say that the growth along [111] direction is kinetically favored at higher temperature in the presence of surfactants and along [100] direction is thermodynamically favored in water. Last but not the least, along with (111) surface exposed ceria, we see more reactive (100) surface exposed single crystalline CeO_2 nanoparticles. This happens due to the fact that the employed temperatures in the present reactions are high enough to promote the formation of {100} facets at the expense of {111} facets.[34,36,37] Therefore, the available (111) and (100) surfaces of the CeO_2 (with lot of surface areas and oxygen storage capacity) will act as the highly active catalytic site[38] in the present case for the oxidation of *para*-xylene to terephthalic acid. In addition, we suggest the possibility of the presence of few CeO_2 nanocrystals exposed in highly active and less stable (110) surfaces from the evidence obtained from the XRD measurements (could not located under HRTEM). Eventually these surfaces will enhance the oxidation of *para*-xylene to terephthalic acid even in mild conditions as suggested by Sayle *et al.*[39] in the support of usefulness of (110) surface containing defects.

Another probable reason of the high surface catalytic activity of the CeO_2 may be due to the presence of CTAB surfactant at the surface. We have confirmed the presence of CTAB at CeO_2 surface by FT-IR spectroscopic measurement. The presence of ionic surfactant is very important, as its ionic end will bind to CeO_2 surface and the tail (hydrophobic) part will have contact with *para*-xylene for oxidation reaction. The presence of CTAB is observed in the recovered CeO_2, reasoning the high catalytic activity even after 3–4 cycles. FT-IR spectra and detail interpretations are given in ESI (Fig. S7†).

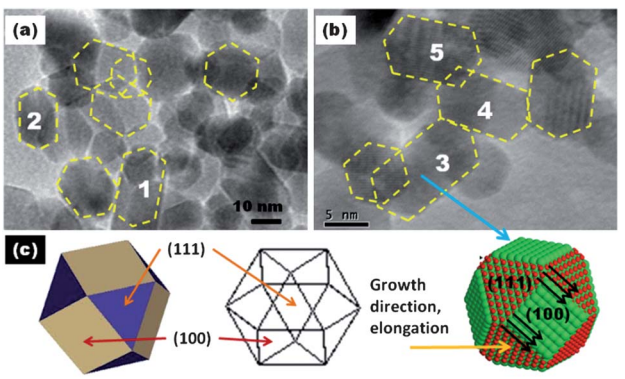

Fig. 8 HRTEM images showing different particles with polyhedral projection, and (bottom) the 3D reconstructions.

Mechanism of *para*-xylene oxidation

Based on the surface structure of the nanocrystalline CeO_2 catalyst, exposed surfaces and surface area described above and the data obtained from HPLC analyses, we proposed a possible mechanism of the catalyst reaction for aerobic oxidation of *para*-xylene for further understanding. Similar to *para*-xylene oxidation with the MC (mid-century) catalyst,[5,40] the present reaction is also believed to occur *via* a free radical chain mechanism, predominantly on the exposed and reactive surfaces of ceria. As shown in eqn (i)–(v), the reaction is initiated *via* the formation of an adduct between adsorbed *para*-xylene (represented as $PhCH_3$) and the active ceria sites, followed by the formation of aralkoxyl ($PhCH_2O^{\cdot}$) radical by the reaction between ceria(III)–$PhCH_3^{+\cdot}$ adduct and molecular oxygen from CeO_2 oxygen vacancies (the increased number of oxygen vacancies on the CeO_2 surface help bind and supply O_2 for the succeeding reactions).[24] In the subsequent step, highly reactive aralkoxyl radical species then abstracts H-atom from *para*-xylene to form aralkyl radical ($PhCH_2^{\cdot}$), which is then oxygenated to peroxyl radical ($PhCH_2OO^{\cdot}$), and the reaction

continues toward the formation of terephthalic acid as shown below.

$$Ce(IV) + 2PhCH_3 \rightarrow 2Ce^{III}\text{–}PhCH_3^{+\cdot} \text{ initiation step} \quad (ii)$$

$$2Ce^{III}\text{–}PhCH_3^{+\cdot} + O_2 \rightarrow Ce(IV) + 2PhCH_2O^{\cdot} + H_2O \quad (iii)$$

$$PhCH_2O^{\cdot} + PhCH_3 \rightarrow PhCH_2OH + PhCH_2^{\cdot} \text{ propagation} \quad (iv)$$

$$PhCH_2^{\cdot} + O_2 \rightarrow PhCH_2OO^{\cdot} \text{ propagation} \quad (v)$$

$$2PhCH_2OO^{\cdot} \rightarrow PhCH_2OH + PhCHO + O_2 \text{ termination} \quad (vi)$$

Thus, the exposed ceria helped to form the free radical rapidly from *para*-xylene by self reduction, which then reacts with oxygen to finally form terephthalic acid.

Conclusion

We have developed a novel heterogeneous catalyst for aqueous phase oxidation of *para*-xylene to bypass all the hazardous steps involved during the production of industrially important terephthalic acid. We have synthesized surface active and (111) and (100) surface exposed CeO_2 nanocrystallite with very high surface area. The particle size of the monodispersed single crystalline particle is 15 nm. XRD and HRTEM analyses confirm the cubic fluorite structure of the ceria nanocrystals, which are grown preferably in ⟨111⟩ and ⟨100⟩ directions due to the presence of surfactants and high temperature, however, exposure of (110) surface in few particles could not be ignored. The catalytic activity of CeO_2 nanocrystals (present samples) was investigated for the first time for aerobic oxidation of *para*-xylene to terephthalic acid in non-hazardous condition. The result shows the formation of 30–40% terephthalic acid under mild reaction condition, *i.e.* at 70 °C in water, by avoiding the corrosive bromide promoter and acetic acid solvent. The recycled catalyst again shows good conversion without the change of the fluorite crystal structure, morphology and the particle size of ceria.

Acknowledgements

KD is grateful to UGC, India and DG is grateful to CSIR, India for research fellowship. SD thanks DST, India for financial support (Grant SR/S1/IC-27/2011). BS thanks University of Delhi and CSIR, India for financial support. We thank Dr T. Ahmad for the help with BET measurements, IIT-Delhi for FESEM, M.Tech. NSNT centre and USIC, DU for XRD and HRTEM facility.

References

1 D. Raju Burri, K. W. Jun, J. S. Yoo, C. W. Lee and S. E. Park, *Catal. Lett.*, 2002, **81**, 169–173.
2 N. M. Emanuel, E. T. Denisov and Z. K. Maizus, *Liquid phase oxidation of Hydrocarbons*, Plenum Press, New York, 1967.
3 Y. Yoshino, Y. Hayashi, T. Iwahama, S. Sakaguchi and Y. Ishii, *J. Org. Chem.*, 1997, **62**, 6810–6813.
4 W. Partenheimer, *Catal. Today*, 1995, **23**, 69–157.
5 B. Saha and J. H. Espenson, *J. Mol. Catal. A: Chem.*, 2007, **271**, 1–5.
6 B. Saha and J. H. Espenson, *J. Mol. Catal. A: Chem.*, 2005, **241**, 33–38.
7 W. P. Schammel, V. Adamian, S. P. Brugge, W. H. Gong, P. D. Metelski, P. O. Nubel and C. Zhou, International Patent WO 133978 A2, 2007.
8 B. Saha, N. Koshino and J. H. Espenson, *J. Phys. Chem. A*, 2004, **108**, 425–531.
9 B. Saha and J. H. Espenson, *J. Mol. Catal. A: Chem.*, 2004, **207**, 123–129.
10 S. A. Chavan, D. Srinivas and P. Ratnasamy, *J. Catal.*, 2001, **204**, 409–419.
11 J. M. Tibbitt, W. H. Gong, W. P. Schammel, R. P. Hepper, V. Adamian, S. P. Brugge, P. D. Metelski and C. Zhou, International Patent WO 2007/133976 A2, 2007.
12 P. A. T. Hamley, T. Ilkenhans, J. M. Webster, E. Garcia-Verdugo, E. Venardou, M. J. Clarke, R. Auerbach, W. B. Thomas, K. Whiston and M. Poliakoff, *Green Chem.*, 2002, **4**, 235–238.
13 S. Chowdhury and K.-S. Lin, *J. Nanomater.*, 2011, **2011**, 1–16.
14 L. Vivier and D. Duprez, *ChemSusChem*, 2010, **3**, 654–678.
15 C. Sun, H. Li and L. Chen, *Energy Environ. Sci.*, 2012, **5**, 8475–8505.
16 C. Kleinlogel and L. Gauckler, *Adv. Mater.*, 2001, **13**, 1081–1085.
17 N. Izu, W. Shin, N. Murayarna and S. Kanzaki, *Sens. Actuators, B*, 2002, **87**, 95–98.
18 S. Rousseau, O. Marie, P. Bazin, M. Daturi, S. Verdier and V. Harle, *J. Am. Chem. Soc.*, 2010, **132**, 10832–10841.
19 M. V. Ganduglia-Pirovano, C. Popa, J. Sauer, H. Abbott, A. Uhl, M. Baron, D. Stacchiola, O. Bondarchuk, K. Shaikhutdinov and H.-J. Freund, *J. Am. Chem. Soc.*, 2010, **132**, 2345–2349.
20 M. Jiang, N. O. Wood and R. Komanduri, *Wear*, 1998, **220**, 59–71.
21 J. Lv, Y. Shen, L. Peng, X. Guo and W. Ding, *Chem. Commun.*, 2010, **46**, 5909–5911.
22 J. Kaspar, P. Fornasiero and M. Graziani, *Catal. Today*, 1999, **50**, 285–298.
23 R. Chockalingam, V. R. W. Amarakoon and H. Giesche, *J. Eur. Ceram. Soc.*, 2008, **28**, 959–963.
24 H. Y. Kim, H. M. Lee and G. Henkelman, *J. Am. Chem. Soc.*, 2012, **134**, 1560–1570.
25 S. Carrettin, P. Concepcion, A. Corma, J. M. Lopez Nieto and V. F. Puntes, *Angew. Chem., Int. Ed.*, 2004, **43**, 2538–2540.
26 A. Bruix, J. A. Rodriguez, P. J. Ramírez, S. D. Senanayake, J. Evans, J. B. Park, D. Stacchiola, P. Liu, J. Hrbek and F. Illas, *J. Am. Chem. Soc.*, 2012, **134**, 8968–8974.
27 D. C. Sayle, S. A. Maicaneanu and G. W. Watson, *J. Am. Chem. Soc.*, 2002, **124**, 11429–11439.
28 (*a*) Q. Wu, F. Zhang, P. Xiao, H. S. Tao, X. Z. Wang, Z. Hu and Y. N. Lu, *J. Phys. Chem. C*, 2008, **112**, 17076–17080; (*b*) X. Liu, K. Zhou, L. Wang, B. Wang and Y. Li, *J. Am. Chem. Soc.*, 2009, **131**, 3140–3141.
29 K. S. W. Sing, D. H. Everett, R. A. W. Haul, L. Moscou, R. A. Pierotti, J. Rouquerol and T. Siemieniewska, *Pure Appl. Chem.*, 1985, **57**, 603–619.

30 E. Mamontov, T. Egami, R. Brezny, M. Koranne and S. Tyagi, *J. Phys. Chem. B*, 2000, **104**, 11110–11116.
31 Z. Wu, M. Li, J. Howe, H. M. Meyer III and S. H. Overbury, *Langmuir*, 2010, **26**, 16595–16606.
32 T. X. T. Sayle, S. C. Parker and C. R. A. Catlow, *Surf. Sci.*, 1994, **316**, 329–336.
33 H. Norenberg and J. H. Harding, *Surf. Sci.*, 2001, **477**, 17–24.
34 F. Dang, K. Kato, H. Imai, S. Wada, H. Haneda and M. Kuwabara, *Cryst. Growth Des.*, 2010, **10**, 4537–4541.
35 N. V. Skorodumova, M. Baudin and K. Hermansson, *Phys. Rev. B: Condens. Matter Mater. Phys.*, 2004, **69**, 075401.
36 A. S. Barnard and S. P. Russo, *J. Phys. Chem. C*, 2009, **113**, 5376–5380.
37 E. D. Leite and C. Ribeiro, *Crystallization and Growth of Colloidal Nanocrystals: Springer Briefs in Materials*, Springer, New York, 2012, pp. 83–89.
38 R. Krahne, G. Morello, A. Figuerola, C. George, S. Deka and L. Manna, *Phys. Rep.*, 2011, **501**, 75–221.
39 T. X. T. Sayle, S. C. Parker and C. R. A. Catlow, *Surf. Sci.*, 1994, **316**, 329–336.
40 (*a*) I. V. Zakharov, Y. V. Geletii and V. A. Adamian, *Kinet. Catal.*, 1991, **32**, 31–37; (*b*) I. V. Zakharov, Y. V. Geletii and V. A. Adamian, *Kinet. Catal.*, 1988, **29**, 924–929.